

Optimization of Magnetic Milli-Spinner for Robotic Endovascular Intervention

*Lu Lu, Luca Higgins, Jack Bernardo, Ruike Renee Zhao**

L. Lu, L. Higgins, J. Bernardo, R. R. Zhao

Department of Mechanical Engineering, Stanford University, Stanford, CA 94305, United States

Email: rrzhao@stanford.edu (R.R. Zhao)

Keywords: Magnetic milli-spinner; Robotic navigation; Design optimization; Propulsion efficiency; Clot debulking.

Abstract

Vascular diseases such as atherosclerosis, thrombosis, and aneurysms can lead to life-threatening medical events. Conventional catheter- or guidewire-based endovascular diagnostic and therapeutic devices often struggle to navigate through highly tortuous vascular pathways. The recently developed multifunctional magnetic milli-spinner offers a promising wireless solution by integrating a central through-hole and side slits into a cylindrical body with helical fins, enabling rapid and stable navigation in complex vascular environments for clot debulking, targeted drug delivery, and aneurysm treatment. Here, we combine computational fluid dynamics simulations with experimental validation to optimize the milli-spinner's structural design for high-speed untethered navigation and high-efficiency clot debulking in tubular flow environments. By systematically examining the effects of through-hole radius, fin number, fin helical angle, and slit dimension on propulsion performance, the optimized magnetic milli-spinner achieves a swimming speed of 55 cm/s (~175 body lengths per second), far exceeding existing untethered magnetic robots in tubular environments (< 80 body lengths per second). This exceptional speed enables stable upstream operation against strong physiological flows representative of major arteries and veins, establishing the magnetic milli-spinner as a robust untethered navigation platform for operation in high-flow, tortuous vasculature, with potential applications in robotic mechanical thrombectomy, embolectomy, and targeted drug delivery.

1. Introduction

In recent decades, catheter- and guidewire-based interventional devices have become the primary tools for the diagnosis and treatment of life-threatening vascular diseases, including thrombosis, aneurysms, and atherosclerosis, which are highly prevalent among middle-aged and elderly populations [1-3]. For example, mechanical thrombectomy employs aspiration catheters and stent retrievers to remove intravascular clots [4, 5], while balloon catheters are widely used to dilate stenotic vessels [6, 7]. These devices are typically introduced via the femoral or radial artery and advanced to the target site through the vasculature. However, navigating such devices through highly tortuous pathways, such as cerebral arteries, remains extremely challenging, and many patients cannot be treated because the devices are unable to reach the disease site. In addition, excessive manipulation during catheter navigation poses a significant risk of vessel injury, including endothelial denudation and, in severe cases, vascular perforation.

Magnetically actuated milli-scale robots [8-12] offer a promising wireless strategy to overcome the limitations of catheter- and guidewire-based interventions by enabling controlled locomotion and guidance under externally applied magnetic fields. Among a variety of magnetic micro- and milli-robot designs for endovascular applications [11-16], propulsion in confined tubular environments is most commonly achieved using propeller-inspired helical structures [17-20] driven by rotating magnetic fields. Building on this concept, Wu et al. [21] recently introduced a magnetic milli-spinner featuring a cylindrical body with helical fins, a central through-hole, and side slits. This unique architecture enables rapid, stable, and fully wireless navigation in highly tortuous vascular networks, while the central through-hole allows blood to pass through the milli-spinner, thereby avoiding vessel occlusion. Beyond locomotion, the magnetic milli-spinner serves as a versatile platform for multifunctional endovascular procedures (**Figure 1a**), including efficient clot debulking, targeted drug delivery, and in situ aneurysm embolization, under magnetic actuation. Notably, the incorporation of the central through-hole and side slits generates a large pressure drop within the milli-spinner during rotation. This pressure drop plays a critical role in enabling high-speed propulsion against physiological blood flow by reducing hydrodynamic resistance and enhancing propulsion efficiency. Moreover, the same pressure gradient produces a highly localized suction field that firmly draws thrombus onto the milli-spinner surface, enabling effective clot debulking. Under high-frequency rotation, the resulting compression and shear

forces induce fibrin-network densification, thereby shrinking the clot volume and facilitating efficient removal [21-23].

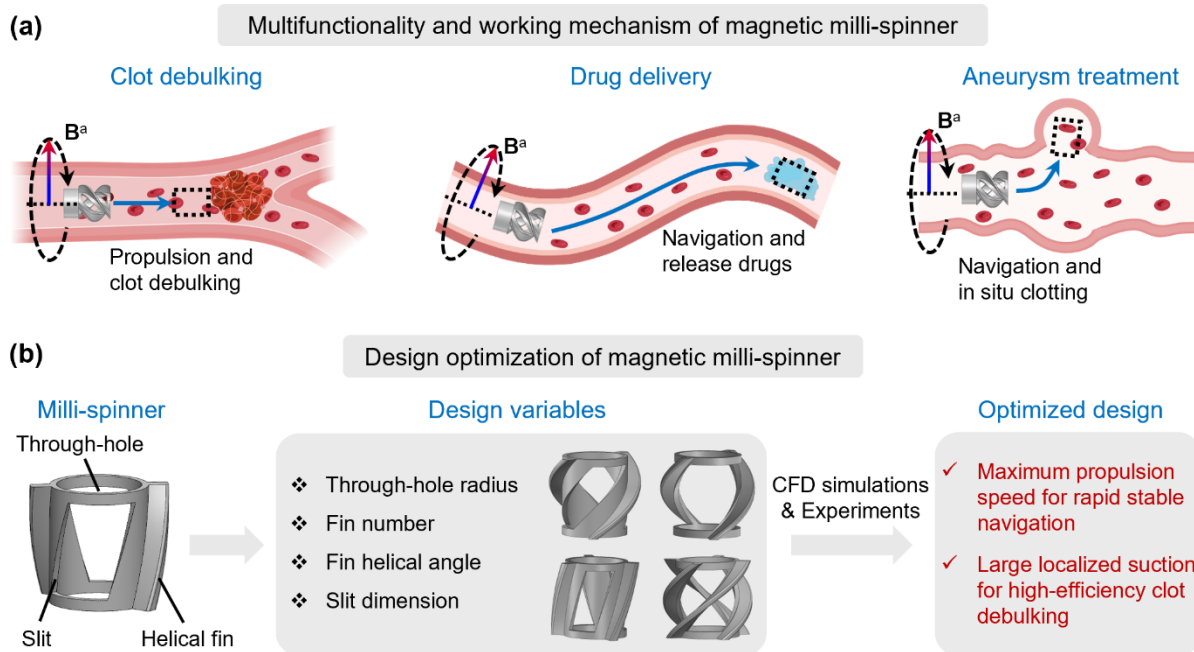


Figure 1. Multifunctional magnetic milli-spinner. (a) Multifunctionality and working mechanism of magnetic milli-spinner in complex vascular environments. (b) Design optimization of magnetic milli-spinner.

The high propulsion efficiency and clot debulking performance of the magnetic milli-spinner arise from the synergistic effect of three structural features: the through-hole, the slit, and the helical fin (**Figure 1b**). These elements introduce a rich set of tunable design parameters, which provide a vast design space for programming the magnetic milli-spinner's overall performance. Systematic parametric optimization of these parameters is therefore essential to fully exploit this potential. In this work, we aim to maximize the propulsion speed of the magnetic milli-spinner for rapid stable navigation in complex vascular environments with high flow rates, while simultaneously enhancing its internal pressure drop to generate large localized suction for high-efficiency clot debulking. To this end, we combine computational fluid dynamics (CFD) simulations with experimental validation to systematically investigate the effects of key geometric parameters, including through-hole radius, fin number, fin helical angle, and slit dimension, on propulsion efficiency and internal pressure drop. Guided by this parametric study, we identify an optimized magnetic milli-spinner design that achieves a swimming speed of 55 cm/s (~ 175 body

lengths per second), far beyond those of existing untethered magnetic robots in tubular environments (< 80 body lengths per second) [17-21]. This exceptional speed is comparable to the peak flow velocity of ~ 60 cm/s and much higher than the average flow velocity of ~ 20 -30 cm/s in the internal carotid artery [24]. It also substantially exceeds both the peak (~ 40 cm/s) and average (~ 10 -20 cm/s) flow velocities in the inferior vena cava [25], demonstrating that the milli-spinner can stably operate upstream against strong physiological flows representative of major arteries and veins. These results establish the magnetic milli-spinner as a viable platform for wireless endovascular intervention under physiologically relevant high-flow conditions and within highly tortuous vasculature, highlighting its potential as a versatile robotic system for a broad range of endovascular procedures, including robotic mechanical thrombectomy, embolectomy, and targeted drug delivery.

2. Results

As shown in **Figure 1b**, the geometry of the magnetic milli-spinner is defined by a rich set of parameters, including the outer diameter, length, through-hole radius, wall thickness, fin length, fin thickness, fin helical angle, fin number, and slit dimension. Here, we focus on optimizing four key geometric parameters that dominate the propulsion performance: *the through-hole radius*, *fin number*, *fin helical angle*, and *slit dimension*. The remaining parameters are selected based on the fabrication constraints and the intended operating environment. The outer diameter of the milli-spinner is fixed at 2.5 mm to enable operation in vessels such as cerebral and coronary arteries with diameters of 3-5 mm. The length of the milli-spinner is set to 2.15 mm, consistent with our original design [21] for comparison purposes. These two dimensions ensure proper fit and agile steering when navigating vessel bifurcations. The wall thickness and the fin thickness of the milli-spinner are set to 0.12 mm and 0.25 mm, respectively, based on the resolution limits of the 3D printing process. A detailed dimensional illustration of the milli-spinner design is provided in **Figure S1** in the Supporting Information. Notably, the milli-spinner geometry can be readily scaled up or down to accommodate a wide range of vessel sizes.

CFD simulations combined with experimental validation (see **Materials and methods** for details) are performed to systematically evaluate the propulsion performance of different milli-spinner designs. In all simulations and experiments, a ring magnet (1 mm inner diameter, 2 mm

outer diameter, and 1 mm length) is coaxially attached to one end of the milli-spinner using adhesive for magnetic actuation. The milli-spinner is placed inside a long tube with an inner diameter of 3.5 mm filled with water and driven by a rotating magnetic field with a controllable frequency to achieve swimming propulsion. CFD simulations are conducted using COMSOL Multiphysics 6.1 (COMSOL Inc., USA). Zero-pressure boundary conditions are applied at both the inlet and outlet of the tube, as illustrated in **Figure S2** in the Supporting Information, and no-slip wall conditions are imposed on the milli-spinner surface and tube wall. Stationary analysis is performed to determine the steady-state flow field, the pressure profile, and the resulting forces acting on the milli-spinner. To determine the propulsion velocity, an initial velocity is applied to the tube wall and iteratively adjusted until the milli-spinner reaches equilibrium. In the equilibrium state, the axial resultant force (i.e., the stress integration in the longitudinal direction over the milli-spinner's surface) approaches zero, indicating that the prescribed wall velocity corresponds to the magnitude of the milli-spinner's equilibrium propulsion velocity but in the opposite direction. This velocity also represents the maximum constant flow speed that the milli-spinner can overcome.

2.1. Effect of through-hole radius

As stated previously, the geometric feature combining a central through-hole and side slits significantly enhances propulsion efficiency and clot-debulking capability by generating a pressure drop within the milli-spinner. Moreover, the through-hole serves as a flow channel that allows blood to pass through the milli-spinner, thereby preventing vessel occlusion. We therefore begin design optimization by examining the effect of the through-hole radius. As shown in **Figure 2a**, with the milli-spinner's outer diameter fixed at 2.5 mm, the through-hole radius-to-fin length ratio, R_{in}/L_{fin} , is selected as the design parameter and varied from 0.5 to 4. Three fin numbers are considered, i.e., $N = 2, 3,$ and 4. For all cases, the fin helical angle is fixed at 30° , which lies within the typical range ($20\text{-}40^\circ$) used in propeller designs [26]. In addition, the slit number equals the fin number. Each slit has two long edges parallel to the helical fin and two short edges parallel to the cylinder ends, with a fixed distance of 1.75 mm between the two short edges (**Figure 2a**). The width of the short edge of a single slit is adjusted according to the fin number to maintain a constant total slit width of 1.83 mm (see details in **Section S1** and **Figure S1** in the Supporting Information).

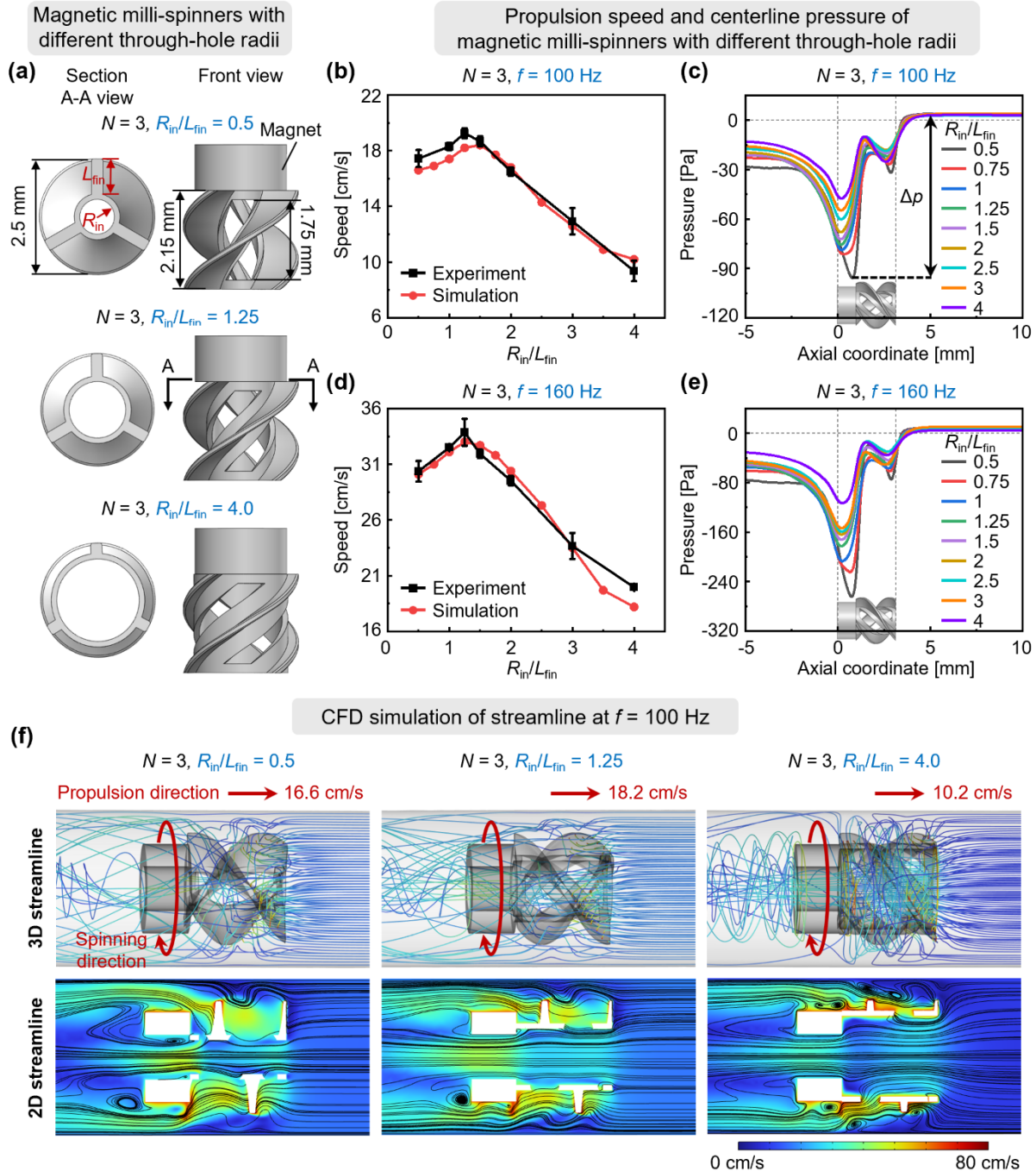


Figure 2. Effect of the through-hole radius on the propulsion performance of 3-fin magnetic milli-spinners operating in a 3.5 mm-diameter tube. (a) Schematics of 3-fin milli-spinners with different through-hole radius-to-fin length ratios R_{in}/L_{fin} . (b) Propulsion speed and (c) centerline pressure of 3-fin milli-spinners with different R_{in}/L_{fin} operating in a 3.5 mm-diameter tube under a rotating magnetic field with frequency $f = 100$ Hz. (d) Propulsion speed and (e) centerline pressure of 3-fin milli-spinners with different R_{in}/L_{fin} operating in a 3.5 mm-diameter tube under a rotating magnetic field with frequency $f = 160$ Hz. (f) 3D streamlines starting from the tube inlet and 2D streamlines on the longitudinal cut plane for 3-fin milli-spinners with different R_{in}/L_{fin} at $f = 100$ Hz.

The effect of the through-hole radius on the propulsion performance of 3-fin magnetic milli-spinners operating inside a 3.5 mm-diameter tube under a rotating magnetic field is investigated in **Figure 2** through CFD simulations and experimental validation. Two rotating-field frequencies, $f = 100$ Hz and 160 Hz, are examined for actuation. As shown in **Figures 2b** and **2d**, at both frequencies, the simulations predict that the propulsion speed of the milli-spinner first increases and then decreases as the through-hole radius increases, reaching maximum values of 18.4 cm/s and 33.0 cm/s at $R_{in}/L_{fin} = 1.5$ and 1.25 for $f = 100$ Hz and 160 Hz, respectively. The experimental results show a similar nonmonotonic trend, with maximum speeds of 19.3 ± 0.35 cm/s and 33.9 ± 1.21 cm/s at $f = 100$ Hz and 160 Hz, respectively, when $R_{in}/L_{fin} = 1.25$. In particular, the speed at 160 Hz is 47.4% higher than the maximum speed of 23.0 cm/s achieved by our original design with the same outer diameter and length [21], highlighting the critical role of design optimization in enhancing the milli-spinner's propulsion efficiency. Experimental demonstrations of the propulsion performance of 3-fin magnetic milli-spinners with $R_{in}/L_{fin} = 0.5, 1.25,$ and 4.0 are shown in **Figure 3** and **Movie S1** in the Supporting Information. The measured speeds of the three designs at $f = 160$ Hz are 30.8 cm/s, 35.0 cm/s, and 20.1 cm/s, respectively. As expected, the milli-spinner with $R_{in}/L_{fin} = 1.25$ travels a longer distance than the other two designs within the same time interval. Combining the simulation and experimental results, the optimal through-hole radius for the 3-fin milli-spinner to achieve the maximum propulsion speed is $R_{in}/L_{fin} = 1.25$.

The centerline pressure along the milli-spinner at the two frequencies predicted by CFD simulations is shown in **Figures 2c** and **2e**. In all cases, a pressure drop Δp (i.e., the difference between the pressure at the distal end of the milli-spinner front and the lowest pressure within the milli-spinner) is observed inside the milli-spinner, resulting from the combined effects of the through-hole and the slits. At both frequencies, Δp decreases monotonically as R_{in}/L_{fin} increases from 0.5 to 4, indicating that a smaller through-hole combined with longer fins produces a higher pressure drop and thereby generates larger localized suction for high-efficiency clot debulking. The optimal through-hole radius for maximum pressure drop differs from that for maximum propulsion speed. Since the primary focus of this study is to improve the propulsion efficiency of the milli-spinner, the optimal through-hole radius for 3-fin magnetic milli-spinners is selected as $R_{in}/L_{fin} = 1.25$.

It should be noted that the ring magnet used to actuate the milli-spinner has a significant influence on both the propulsion speed and centerline pressure. **Figure S3** in the Supporting Information presents the propulsion speed and centerline pressure of 3-fin milli-spinners without the ring magnet for different through-hole radii based on CFD simulations. The results show that the ring magnet decreases the propulsion speed but increases the pressure drop of the milli-spinner. This suggests that the propulsion efficiency of the milli-spinner could be further improved by optimizing the actuation method, for example, by directly fabricating the milli-spinner using magnetic soft materials [27].

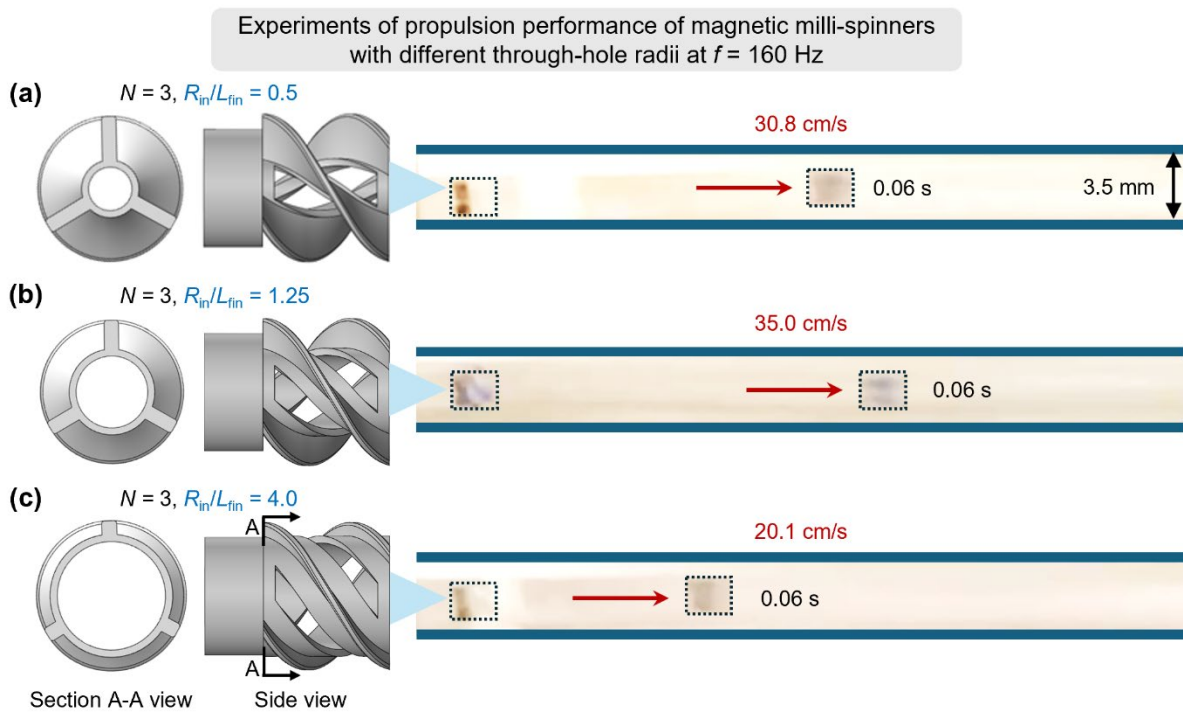


Figure 3. Experiments of propulsion performance of 3-fin magnetic milli-spinners with different through-hole radii operating in a 3.5 mm-diameter tube under a 160 Hz rotating magnetic field. (a) $R_{in}/L_{fin} = 0.5$. (b) $R_{in}/L_{fin} = 1.25$. (c) $R_{in}/L_{fin} = 4$. Experimental results demonstrate that the 3-fin milli-spinner achieves the highest propulsion speed when the through-hole radius-to-fin length ratio is $R_{in}/L_{fin} = 1.25$.

To elucidate the distinct effects of R_{in}/L_{fin} on the propulsion efficiency of magnetic milli-spinners, **Figure 2f** compares the CFD-predicted 2D and 3D streamlines in the tube for different through-hole radii at $f = 100$ Hz. For small or large through-hole radii (e.g., $R_{in}/L_{fin} = 0.5$ and 4), strong vortices are observed near the tube wall and at the rear of the milli-spinner during spinning motion, as evident in the 2D streamlines, which dissipate energy and reduce propulsion efficiency. In contrast, with an intermediate through-hole radius (e.g., $R_{in}/L_{fin} = 1.25$), the spinning motion

generates more coherent axial streamlines, leading to a continuous high-velocity region in the tube, as shown in the 3D streamlines.

Results for 2-fin and 4-fin magnetic milli-spinners with different through-hole radii are provided in **Figures S4** and **S5** in the Supporting Information. The 2-fin milli-spinner achieves its maximum speeds of 18.8 ± 1.0 cm/s and 32.8 ± 0.46 cm/s at $f=100$ Hz and 160 Hz, respectively, when $R_{in}/L_{fin} = 0.5$. The 4-fin milli-spinner reaches its maximum speeds of 14.3 ± 0.20 cm/s and 27.0 ± 0.68 cm/s at $f=100$ Hz and 160 Hz, respectively, when $R_{in}/L_{fin} = 1.5$. Compared with the 3-fin milli-spinner at $R_{in}/L_{fin} = 1.25$ (19.3 ± 0.35 cm/s and 33.9 ± 1.21 cm/s at $f=100$ Hz and 160 Hz, respectively), the 2-fin and 4-fin designs exhibit lower speeds at both frequencies (see experimental demonstrations in **Movie S2** in the Supporting Information). Based on these results, the 3-fin magnetic milli-spinner with $R_{in}/L_{fin} = 1.25$ is selected as the optimized design and is used for subsequent optimizations of the fin helical angle and slit dimension.

2.2. Effect of fin helical angle

Next, we optimize the fin helical angle based on the first-step optimization results of the through-hole radius. Specifically, the fin number and the through-hole radius-to-fin length ratio are fixed at $N=3$ and $R_{in}/L_{fin} = 1.25$, respectively. The width of a single slit is kept constant at 0.61 mm for all cases. To identify the optimal fin helical angle, we compare the propulsion speed and centerline pressure of 3-fin magnetic milli-spinners with helical angles ranging from 20° to 80° (**Figure 4a**) operating in a 3.5 mm-diameter tube. **Figures 4b** and **4d** show the propulsion speeds of milli-spinners with different helical angles under rotating magnetic fields of 100 Hz and 160 Hz, respectively. In both cases, simulations and experiments consistently show that the propulsion speed first increases and then decreases as the helical angle α increases from 20° to 80° , reaching its maximum at $\alpha = 60^\circ$. The maximum experimental speeds are 23.8 ± 0.53 cm/s at $f=100$ Hz and 45.0 ± 1.87 cm/s at $f=160$ Hz, which are enhanced by 23.3% and 32.7%, respectively, compared with the first-step optimized design. Experimental demonstrations of the propulsion performance of magnetic milli-spinners with $\alpha = 30^\circ$, 60° , and 80° are presented in **Figure 5** and **Movie S3** in the Supporting Information. At $f=160$ Hz, the measured propulsion speeds are 35.0 cm/s, 45.6 cm/s, and 30.0 cm/s for $\alpha = 30^\circ$, 60° , and 80° , respectively. These results confirm that the optimal fin helical angle of 3-fin milli-spinners with $R_{in}/L_{fin} = 1.25$ for achieving the highest propulsion efficiency is $\alpha = 60^\circ$.

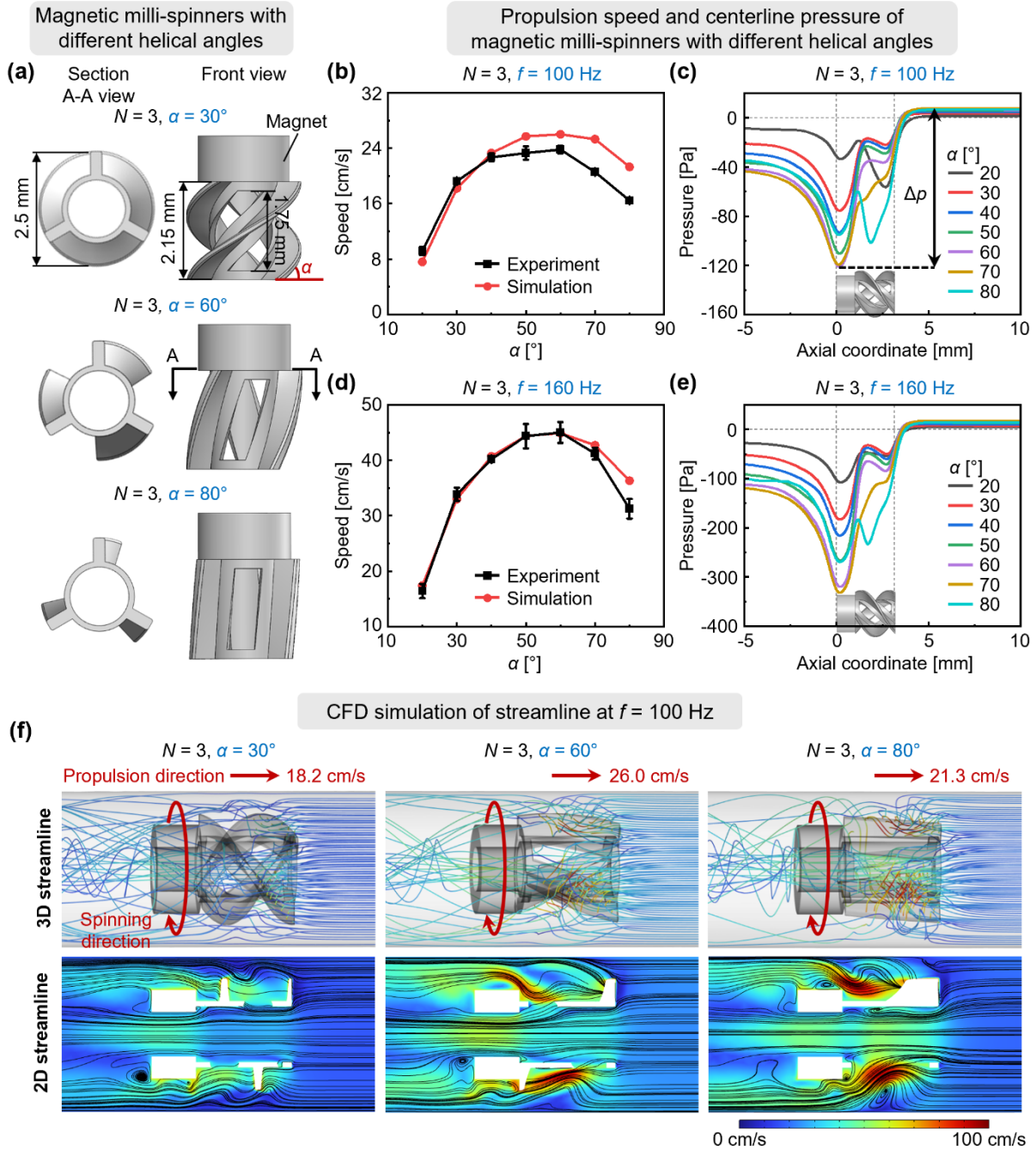


Figure 4. Effect of the fin helical angle on the propulsion performance of 3-fin magnetic milli-spinners with $R_{in}/L_{fin} = 1.25$ operating in a 3.5 mm-diameter tube. (a) Schematics of 3-fin milli-spinners with different fin helical angles α . (b) Propulsion speed and (c) centerline pressure of 3-fin milli-spinners with different helical angles operating in a 3.5 mm-diameter tube under a rotating magnetic field with frequency $f = 100$ Hz. (d) Propulsion speed and (e) centerline pressure of 3-fin milli-spinners with different helical angles operating in a 3.5 mm-diameter tube under a rotating magnetic field with frequency $f = 160$ Hz. (f) 3D streamlines starting from the tube inlet and 2D streamlines along the longitudinal cut plane for 3-fin milli-spinners with different helical angles at $f = 100$ Hz.

The centerline pressure along the milli-spinner inside the tube at the two rotating frequencies predicted by CFD simulations is shown in **Figures 4c** and **4e**. At both frequencies, the pressure drop Δp varies nonmonotonically as α increases from 20° to 80° , with maximum Δp occurring at $\alpha = 60^\circ$ and 70° for $f = 100$ Hz and 160 Hz, respectively. Compared with the first-step optimization of the through-hole radius, the maximum pressure drops increase by 25.0% and 25.3% at the two frequencies after optimizing the fin helical angle, resulting in stronger localized suction and enhanced clot-debulking capability. Notably, the helical angle for maximum propulsion speed is nearly consistent with that for maximum pressure drop. Therefore, the optimal helical angle for 3-fin milli-spinners with $R_{in}/L_{fin} = 1.25$ is selected as $\alpha = 60^\circ$.

The effects of the fin helical angle on the propulsion speed and centerline pressure of 3-fin milli-spinners without a ring magnet are examined using CFD simulations in **Figure S6** in the Supporting Information. As expected, at the same rotating frequency, the milli-spinner without a ring magnet exhibits higher propulsion speed than that with a ring magnet, owing to reduced weight and fluid resistance. In the absence of a ring magnet, the variation trends of both propulsion speed and pressure drop with respect to the helical angle are similar to those observed with a ring magnet. However, the helical angles corresponding to the maximum propulsion speed and maximum pressure drop shift to $\alpha = 50^\circ$ and $\alpha = 70^\circ$, respectively, at both frequencies.

Figure 4f illustrates the CFD-predicted 3D and 2D streamlines inside the tube for different helical angles at $f = 100$ Hz. From the 3D streamlines, it is observed that when the helical angle is relatively small (e.g., $\alpha = 30^\circ$), the spinning-induced flow velocity is noticeably lower than that observed for $\alpha = 60^\circ$ and 80° . In these two cases, the flow passing through the central through-hole and side slits is significantly accelerated, as indicated by the red regions in the 2D streamlines, creating a larger pressure drop that reduces the hydrodynamic resistance and improves the propulsion efficiency. In addition, for $\alpha = 80^\circ$, stronger vortices form near the tube wall. These vortices dissipate energy and decrease propulsion efficiency. As a result, the milli-spinner with $\alpha = 60^\circ$ achieves the highest propulsion speed among the three cases.

Experiments of propulsion performance of magnetic milli-spinners
with different helical angles at $f = 160$ Hz

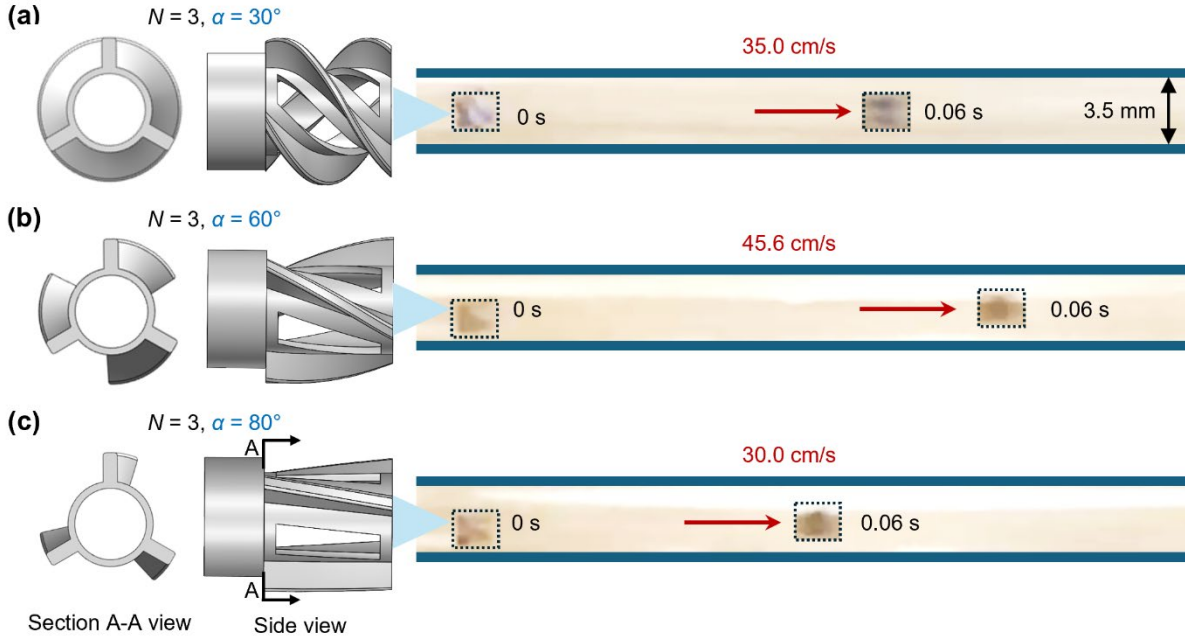


Figure 5. Experiments of propulsion performance of 3-fin magnetic milli-spinners with $R_{in}/L_{fin} = 1.25$ and different fin helical angles operating in a 3.5 mm-diameter tube under a 160 Hz rotating magnetic field. (a) $\alpha = 30^\circ$. (b) $\alpha = 60^\circ$. (c) $\alpha = 80^\circ$. Experimental results demonstrate that the 3-fin milli-spinner with $R_{in}/L_{fin} = 1.25$ achieves the highest propulsion speed when the helical angle is $\alpha = 60^\circ$.

2.3. Effect of slit dimension

In the following, we further optimize the slit dimension by examining its effects on the propulsion speed and centerline pressure of magnetic milli-spinners. Based on the first two-step optimization, the fin number, the through-hole radius-to-fin length ratio, and the fin helical angle are fixed at $N = 3$, $R_{in}/L_{fin} = 1.25$, and $\alpha = 60^\circ$, respectively. As shown in **Figure 6a**, consistent with the slit design used in the previous optimization steps, each slit has two long edges parallel to the helical fin and two short edges parallel to the cylinder ends, with a fixed distance of 1.75 mm between the two short edges. The total width w_T of the short edges of the three slits is normalized by the cylinder centerline circumference $S = 2\pi r$, where r is the centerline radius. This normalized width w_T/S is set as the design variable and varied from 0.25 to 0.875 ($w_T/S = 0.875$ corresponds to the maximum slit width that can be designed for 3-fin milli-spinners with a fin thickness of 0.25 mm).

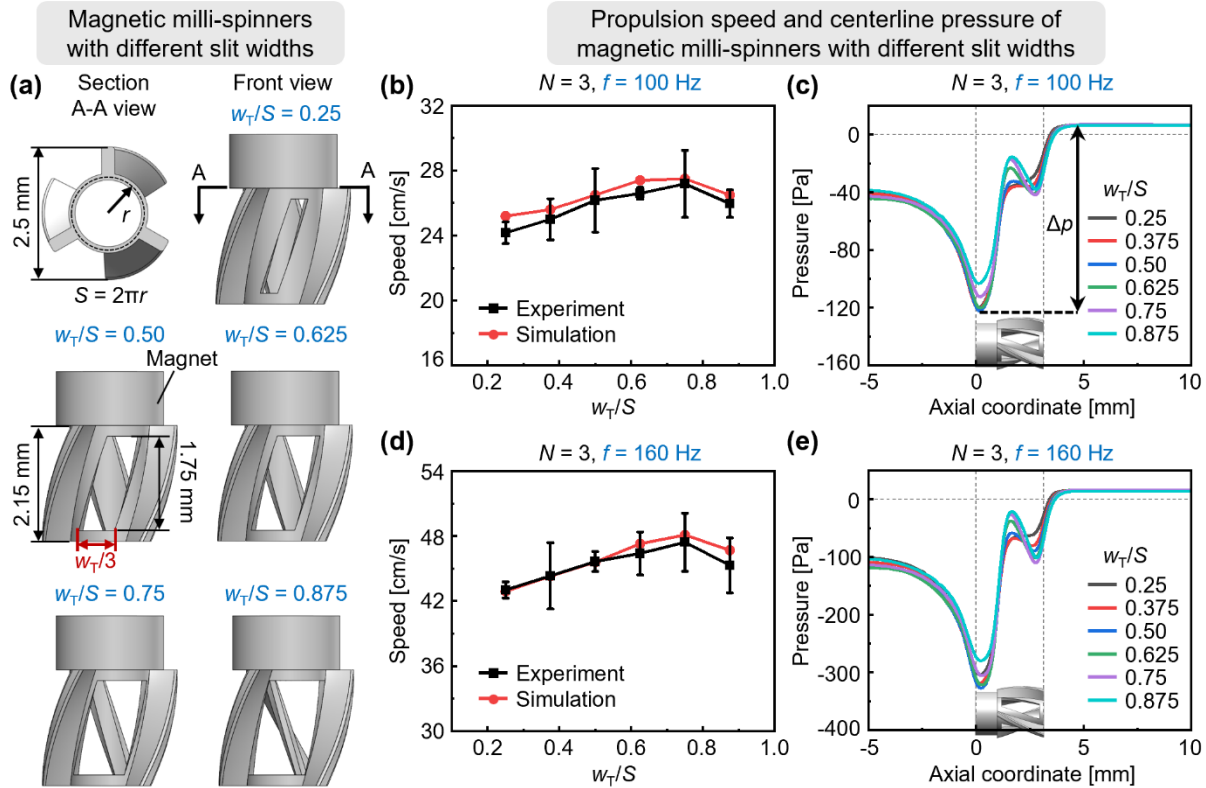


Figure 6. Effect of the slit width on the propulsion performance of 3-fin magnetic milli-spinners operating in a 3.5 mm-diameter tube. (a) Schematics of 3-fin milli-spinners with varying normalized slit width w_T/S . (b) Propulsion speed and (c) centerline pressure of 3-fin milli-spinners with different w_T/S operating in a 3.5 mm-diameter tube under a rotating magnetic field with frequency $f = 100$ Hz. (d) Propulsion speed and (e) centerline pressure of 3-fin milli-spinners with different w_T/S operating in a 3.5 mm-diameter tube under a rotating magnetic field with frequency $f = 160$ Hz.

Figures 6b and **6d** show the propulsion speeds of magnetic milli-spinners with different slit widths operating in a 3.5 mm-diameter tube under rotating magnetic fields of 100 Hz and 160 Hz, respectively. After the first two-step optimization of through-hole radius and fin helical angle, the effect of slit dimension on propulsion efficiency becomes less significant. Both simulations and experiments indicate that the milli-spinner achieves its maximum speed when the normalized slit width w_T/S increases to 0.75 at the two frequencies. The experimental maximum speeds at $f = 100$ Hz and 160 Hz are 27.2 ± 2.06 cm/s and 47.4 ± 2.68 cm/s, respectively, which are enhanced by 14.3% and 5.3% compared with the speeds obtained after optimizing the helical angle. Experimental demonstrations of the propulsion performance of milli-spinners with $w_T/S = 0.25, 0.75, \text{ and } 0.875$ are shown in **Figure 7** and **Movie S4** in the Supporting Information. At $f = 160$ Hz, the measured propulsion speeds for milli-spinners with $w_T/S = 0.25, 0.75, \text{ and } 0.875$ are 43.0

cm/s, 50.3 cm/s, and 44.9 cm/s, respectively. Combining simulation and experimental results, the optimal normalized slit width of 3-fin milli-spinners with $R_{in}/L_{fin} = 1.25$ and $\alpha = 60^\circ$ for achieving the maximum propulsion speed is $w_T/S = 0.75$.

The corresponding centerline pressure along the milli-spinner inside the tube for different slit widths at $f = 100$ Hz and 160 Hz are shown in **Figures 6c** and **6e**, respectively. Similar to the propulsion speed, the pressure drop exhibits a relatively weak dependence on slit width after optimization of the through-hole radius and fin helical angle. For both frequencies, the pressure drop reaches its maximum at $w_T/S = 0.5$. As the primary objective is to maximize the propulsion efficiency, the optimal normalized slit width of 3-fin milli-spinners with $R_{in}/L_{fin} = 1.25$ and $\alpha = 60^\circ$ is therefore selected as $w_T/S = 0.75$, which is also the final optimized design after the three-step optimization. It should be noted that, although the slit width has a relatively minor effect on the propulsion speed and internal pressure drop of the milli-spinner with optimized through-hole radius and fin helical angle, a larger slit width contributes to a higher drug delivery rate by providing a larger area for fluid exchange between the drug within the internal cavity and the surrounding environment [21]. Therefore, for applications involving drug delivery, a larger slit width may be considered in the milli-spinner design.

The effects of slit dimension on the propulsion speed and centerline pressure of milli-spinners without a ring magnet are studied in **Figure S7** in the Supporting Information using CFD simulations. In this case, the propulsion speed also becomes less sensitive to the slit width after the first two-step optimization, but the speed is increased by approximately 20% compared to milli-spinners with a ring magnet. However, in the absence of a ring magnet, the pressure drop decreases monotonically with increasing slit width, suggesting that narrower slits lead to a higher pressure drop, which generates larger localized suction that facilitates clot debulking.

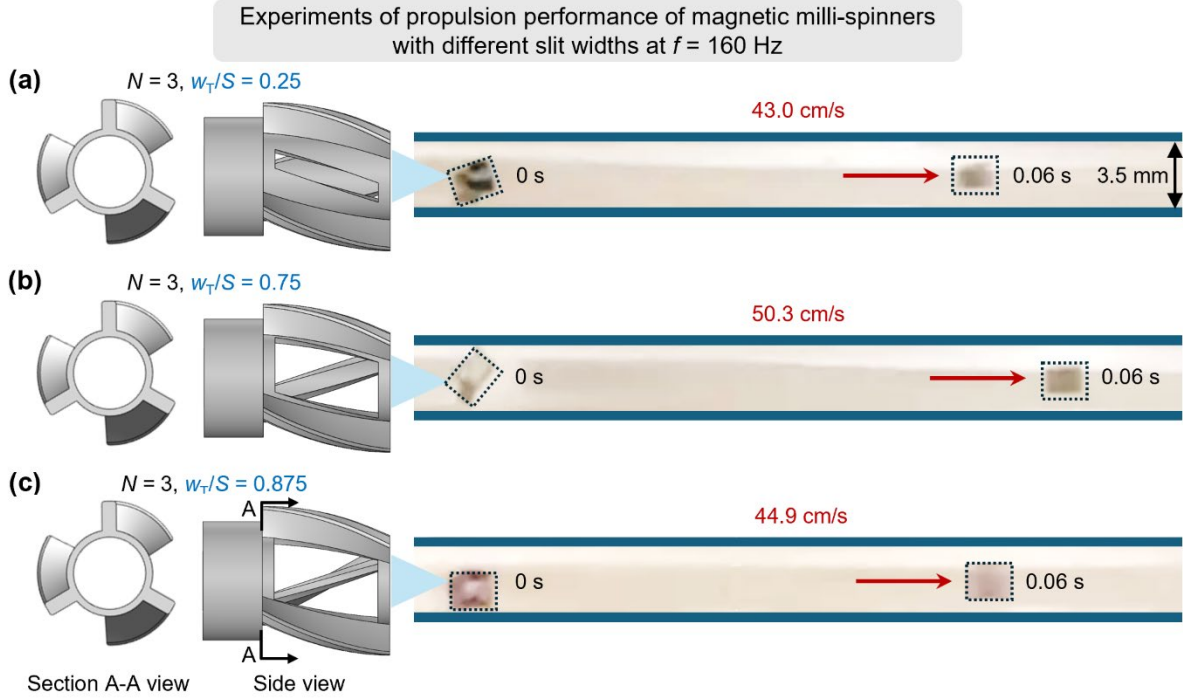


Figure 7. Experiments of 3-fin magnetic milli-spinners with different slit widths operating in a 3.5 mm-diameter tube under a 160 Hz rotating magnetic field. (a) $w_T/S = 0.25$. (b) $w_T/S = 0.75$. (c) $w_T/S = 0.875$. Experimental results demonstrate that the 3-fin milli-spinner with $R_{in}/L_{fin} = 1.25$ and $\alpha = 60^\circ$ achieves the highest propulsion speed when the normalized slit width is $w_T/S = 0.75$.

2.4. Optimized magnetic milli-spinner for high-efficiency propulsion and clot debulking

Finally, we evaluate the propulsion efficiency of the optimized magnetic milli-spinner (**Figure 8a**) at different rotating frequencies, as well as its clot debulking capability for robotic mechanical thrombectomy. **Figures 8b** and **8c** present the propulsion speed and centerline pressure of the optimized milli-spinner operating in a tube with an inner diameter of 3.5 mm at various rotating frequencies. Both simulations and experiments show that the propulsion speed and pressure drop increase nearly linearly with the rotating frequency, indicating that higher frequencies enhance both propulsion efficiency and clot-debulking capability. At $f = 180$ Hz (the highest frequency achievable with our coil system), the maximum experimental speed reaches 55 cm/s (~ 175 body lengths per second), far beyond those of existing untethered magnetic robots in tubular environments (< 80 body lengths per second) [17-21]. This exceptional speed is comparable to the peak flow velocity of ~ 60 cm/s and much higher than the average flow velocity of ~ 20 -30 cm/s in the internal carotid artery [24]. It also substantially exceeds both the peak (~ 40 cm/s) and average (~ 10 -20 cm/s) flow velocities in the inferior vena cava [25], demonstrating that

the optimized magnetic milli-spinner can stably operate upstream against strong physiological flows representative of major arteries and veins. Experimental demonstration of the maximum propulsion speed is shown in **Figure 8d** and **Movie S5** in the Supporting Information. Note that by increasing the rotating frequency (**Figure 8b**) or by fabricating the milli-spinner using magnetic soft materials [27], much higher propulsion speed can be achieved. These results suggest that the optimized magnetic milli-spinner is capable of performing medical tasks in vascular environments with high flow rates.

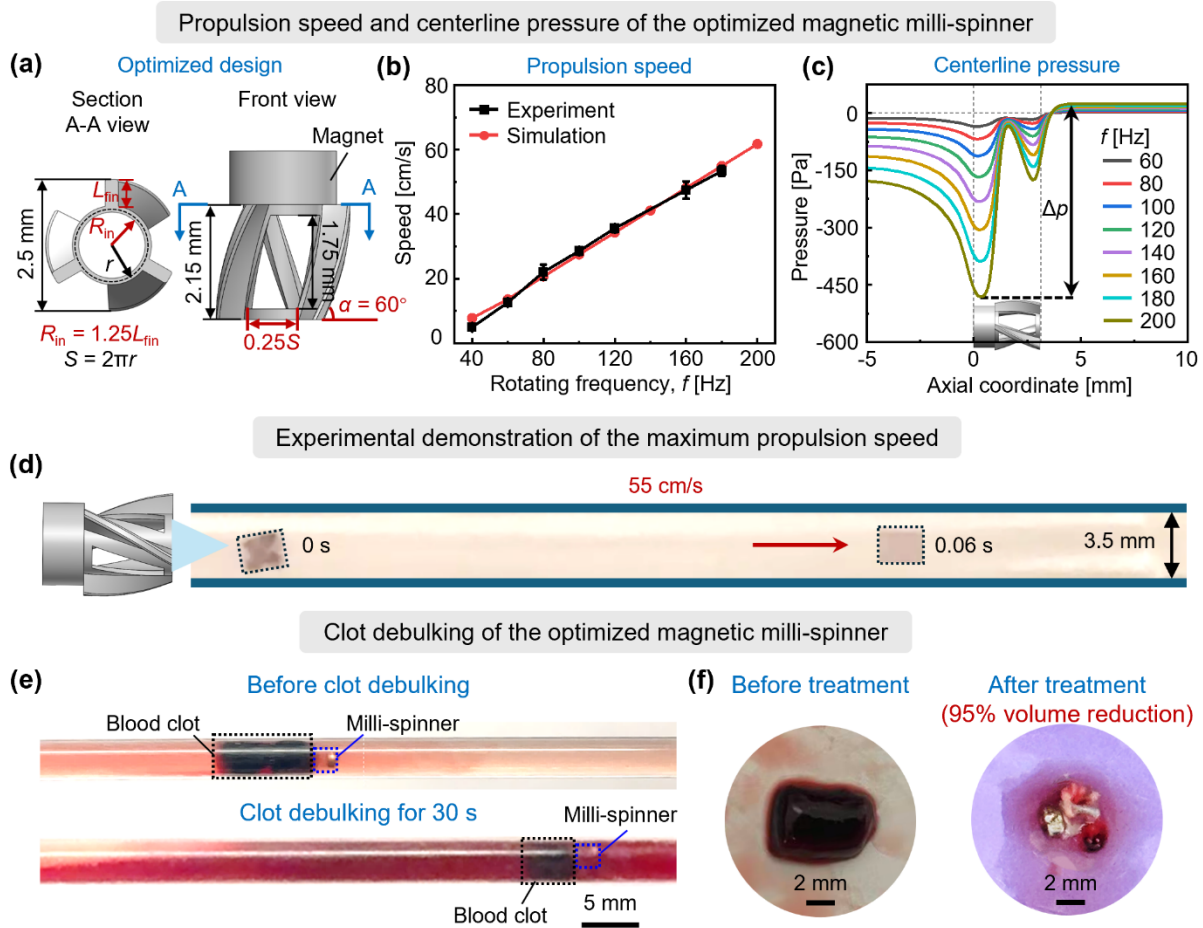


Figure 8. Propulsion performance and clot debulking of the optimized magnetic milli-spinner. (a) Schematic of the optimized magnetic milli-spinner design. (b) Propulsion speed and (c) centerline pressure of the optimized magnetic milli-spinner operating in a 3.5 mm-diameter tube under rotating magnetic fields with different frequencies. (d) Experimental demonstration of the maximum propulsion speed of the optimized magnetic milli-spinner at $f = 180$ Hz. (e) Clot debulking of the optimized magnetic milli-spinner. (f) Experimental images of the whole blood clot before and after treatment. After treatment, the clot transforms into a highly densified white fibrin core and exhibits an approximately 95% reduction in volume.

Figure 8e demonstrates the clot debulking performance of the optimized magnetic milli-spinner in a tubular environment under a 160 Hz rotating magnetic field. The milli-spinner first propels itself to the whole blood clot, after which the clot is drawn against the milli-spinner due to the suction force generated by the internal pressure drop. Simultaneously, the milli-spinner's rotation applies a continuous shear force to the clot. The combined compression and shear forces result in drastic densification and collapse of the fibrin network while releasing red blood cells [21-23], reducing the clot volume by approximately 50% within 30 s. Simultaneously, the strong suction force draws the entire clot proximally during the debulking process, effectively anchoring it and preventing distal migration or washout by physiological blood flow under realistic operating conditions. With continued treatment, the clot volume is ultimately reduced by approximately 95%, and the clot transforms into a highly densified white fibrin core, as shown in **Figure 8f**, demonstrating the high-efficiency clot-debulking capability of the optimized magnetic milli-spinner.

3. Conclusion

In summary, we performed design optimization for magnetic milli-spinners featuring a cylindrical body with a central through-hole, side slits, and helical fins through a combination of computational fluid dynamics simulations and experimental validation. To identify the optimized design, we systematically investigated the effects of several key parameters, including through-hole radius, fin number, fin helical angle, and slit dimension, on the propulsion performance of magnetic milli-spinners operating in a tubular environment under a rotating magnetic field. Both simulations and experiments demonstrate that these parameters play critical roles in enhancing the propulsion speed and internal pressure drop of magnetic milli-spinners. By rationally selecting these parameters, an optimized milli-spinner design is proposed, which achieves a propulsion speed of 55 cm/s (~175 body lengths per second) under a rotating magnetic field of 180 Hz and 20 mT, far beyond those of existing untethered magnetic robots in tubular environments (< 80 body lengths per second). This exceptional speed is comparable to the peak flow velocity of ~60 cm/s and much higher than the average flow velocity of ~20-30 cm/s in the internal carotid artery, which also substantially exceeds both the peak (~40 cm/s) and average (~10-20 cm/s) flow velocities in the inferior vena cava. Such high propulsion efficiency enables wireless operation in tortuous

vascular environments with high flow rates, opening new opportunities for magnetic milli-spinners in a broad range of endovascular procedures, including robotic mechanical thrombectomy, embolectomy, and targeted drug delivery.

4. Materials and methods

4.1. Computational fluid dynamics simulations

To qualitatively evaluate the propulsion performance of magnetic milli-spinners with various design parameters in tubular environments, CFD simulations are conducted using COMSOL Multiphysics 6.1 (COMSOL Inc., USA). The Reynolds number in the tubular system is defined as $Re = UD/\nu$ [28], where $U = \pi fD$ is the characteristic velocity, with f and D representing the rotating frequency and the outer diameter of the milli-spinner, respectively, and $\nu = 1.0 \times 10^{-6}$ m²/s is the kinematic viscosity of water at 20 °C. The highest rotating frequency considered in the simulation is 200 Hz, corresponding to a Reynolds number of 3927, which is below the turbulent regime (typically $Re > 4000$). As a result, the laminar flow model combined with a frozen motor method is employed in all simulations. In the frozen rotor method, a cylindrical rotating domain, slightly larger than the magnetic milli-spinner, is defined, with a rotational velocity prescribed along its longitudinal axis. Moreover, zero-pressure boundary conditions are applied at both the inlet and outlet, and no-slip wall conditions are imposed on the milli-spinner surface and tube wall. To minimize the influence of boundary effects, a 300 mm long tube filled with water is used as the computational flow domain. Stationary analysis is performed to determine the steady-state flow field, pressure profile, and the resulting forces acting on the milli-spinner. In particular, the axial force on the magnetic milli-spinner is calculated by integrating the stress in the longitudinal direction over its surface. To estimate the equilibrium propulsion velocity generated by this force, an initial velocity is specified for the tube wall and iteratively adjusted until the milli-spinner reaches equilibrium. In the equilibrium state, the computed axial force approaches zero (values below 10^{-6} N are considered negligible), indicating that the prescribed tube wall velocity corresponds to the magnitude of the milli-spinner's equilibrium propulsion velocity but in the opposite direction.

4.2. Experiments

The CFD-predicted propulsion speeds of magnetic milli-spinners are validated experimentally. In the experiments, the milli-spinner body is fabricated using a customized digital light processing (DLP) 3D printer, with ANYCUBIC ABS-Like Resin 3.0 as the printing material. A ring-shaped neodymium magnet (grade N50, SM Magnetics, USA) with an inner diameter of 1 mm, outer diameter of 2 mm, and length of 1 mm is attached to one end of the milli-spinner using adhesive. When subjected to a rotating magnetic field, the ring magnet drives the milli-spinner to rotate, thereby generating propulsion in the fluid. The rotating magnetic field is produced by a three-axis Helmholtz coil system (see **Section S2** and **Figure S8** in the Supporting Information for details of the experimental setup and magnetic actuation). Propulsion tests are conducted in a water-filled tube with an inner diameter of 3.5 mm and a length of 100 mm, positioned within the working space of the Helmholtz coil system. The magnetic milli-spinner is initially placed at one end of the tube and swims to the other end upon application of a rotating magnetic field. To achieve stable propulsion, a magnetic field strength of 15 mT is employed for rotating frequencies $f \leq 160$ Hz, whereas 20 mT is used at frequencies $f > 160$ Hz. The entire propulsion process is recorded using a camera, from which the displacement-time curve is extracted. The slope of the linear portion of this curve is taken as the equilibrium velocity of the magnetic milli-spinner.

References

- [1] N. Mackman, "Triggers, targets and treatments for thrombosis," *Nature*, vol. 451, no. 7181, pp. 914-918, 2008.
- [2] J. L. Björkegren, and A. J. Lusis, "Atherosclerosis: recent developments," *Cell*, vol. 185, no. 10, pp. 1630-1645, 2022.
- [3] N. Sakalihasan, J.-B. Michel, A. Katsargyris, H. Kuivaniemi, J.-O. Defraigne, A. Nchimi, J. T. Powell, K. Yoshimura, and R. Hultgren, "Abdominal aortic aneurysms," *Nature Reviews Disease Primers*, vol. 4, no. 1, pp. 34, 2018.
- [4] S. A. Munich, K. Vakharia, and E. I. Levy, "Overview of mechanical thrombectomy techniques," *Neurosurgery*, vol. 85, pp. S60-S67, 2019.
- [5] G. Gascou, K. Lobotesis, P. Machi, I. Maldonado, J. Vendrell, C. Riquelme, O. Eker, G. Mercier, I. Mourand, and C. Arquizan, "Stent retrievers in acute ischemic stroke: complications and failures during the perioperative period," *American Journal of Neuroradiology*, vol. 35, no. 4, pp. 734-740, 2014.
- [6] B. Scheller, C. Hehrlein, W. Bocksch, W. Rutsch, D. Haghi, U. Dietz, M. Böhm, and U. Speck, "Treatment of coronary in-stent restenosis with a paclitaxel-coated balloon catheter," *New England Journal of Medicine*, vol. 355, no. 20, pp. 2113-2124, 2006.

- [7] F. Alfonso, and B. Scheller, “State of the art: balloon catheter technologies-drug-coated balloon,” *EuroIntervention*, vol. 13, no. 6, pp. 680-695, 2017.
- [8] Q. Wang, Z. Zhang, B. Li, J. Wang, and H. Gu, “Hard-Magnetic Soft Millirobots in Underactuated Systems,” *Advanced Robotics Research*, pp. 202500071, 2025.
- [9] Z. Ren, and M. Sitti, “Design and build of small-scale magnetic soft-bodied robots with multimodal locomotion,” *Nature Protocols*, vol. 19, no. 2, pp. 441-486, 2024.
- [10] Z. Yang, H. Yang, Y. Cao, Y. Cui, and L. Zhang, “Magnetically actuated continuum medical robots: A review,” *Advanced Intelligent Systems*, vol. 5, no. 6, pp. 2200416, 2023.
- [11] Q. Ze, S. Wu, J. Dai, S. Leanza, G. Ikeda, P. C. Yang, G. Iaccarino, and R. R. Zhao, “Spinning-enabled wireless amphibious origami millirobot,” *Nature Communications*, vol. 13, pp. 3118, 2022.
- [12] Q. Ze, S. Wu, J. Nishikawa, J. Dai, Y. Sun, S. Leanza, C. Zemelka, L. S. Novelino, G. H. Paulino, and R. R. Zhao, “Soft robotic origami crawler,” *Science Advances*, vol. 8, no. 13, pp. eabm7834, 2022.
- [13] N. J. Greenidge, B. Calmé, A. C. Moldovan, B. Abaravicius, J. W. Martin, N. Marahrens, J. Woolfrey, B. Scaglioni, D. S. Chaturanga, and S. Mitra, “Harnessing the oloid shape in magnetically driven robots to enable high-resolution ultrasound imaging,” *Science Robotics*, vol. 10, no. 100, pp. eadq4198, 2025.
- [14] X. Liu, L. Wang, Y. Xiang, F. Liao, N. Li, J. Li, J. Wang, Q. Wu, C. Zhou, and Y. Yang, “Magnetic soft microfiberbots for robotic embolization,” *Science Robotics*, vol. 9, no. 87, pp. eadh2479, 2024.
- [15] M. Zhang, L. Yang, H. Yang, L. Su, J. Xue, Q. Wang, B. Hao, Y. Jiang, K. F. Chan, and J. J. Y. Sung, “A magnetically actuated microcatheter with soft rotatable tip for enhanced endovascular access and treatment efficiency,” *Science Advances*, vol. 11, no. 25, pp. eadv1682, 2025.
- [16] R. Dreyfus, Q. Boehler, S. Lyttle, P. Gruber, J. Lussi, C. Chautems, S. Gervasoni, J. Berberat, D. Seibold, and N. Ochsenbein-Kölble, “Dexterous helical magnetic robot for improved endovascular access,” *Science Robotics*, vol. 9, no. 87, pp. eadh0298, 2024.
- [17] Q. Wang, X. Du, D. Jin, and L. Zhang, “Real-time ultrasound doppler tracking and autonomous navigation of a miniature helical robot for accelerating thrombolysis in dynamic blood flow,” *ACS Nano*, vol. 16, no. 1, pp. 604-616, 2022.
- [18] A. C. Bakenecker, A. von Gladiss, H. Schwenke, A. Behrends, T. Friedrich, K. Lütke-Buzug, A. Neumann, J. Barkhausen, F. Wegner, and T. M. Buzug, “Navigation of a magnetic micro-robot through a cerebral aneurysm phantom with magnetic particle imaging,” *Scientific Reports*, vol. 11, no. 1, pp. 14082, 2021.
- [19] S. Jeon, S. Kim, S. Ha, S. Lee, E. Kim, S. Y. Kim, S. H. Park, J. H. Jeon, S. W. Kim, and C. Moon, “Magnetically actuated microrobots as a platform for stem cell transplantation,” *Science Robotics*, vol. 4, no. 30, pp. eaav4317, 2019.
- [20] L.-J. W. Ligtenberg, N. C. Rabou, C. Goulas, W. C. Duinmeijer, F. R. Halfwerk, J. Arens, R. Lomme, V. Magdanz, A. Klingner, and E. A. Klein Rot, “Ex vivo validation of magnetically actuated intravascular untethered robots in a clinical setting,” *Communications Engineering*, vol. 3, no. 1, pp. 68, 2024.
- [21] S. Wu, Y. Chang, S. Leanza, J. Sim, L. Lu, Q. Li, D. Stone, and R. R. Zhao, “Magnetic Milli-Spinner for Robotic Endovascular Surgery,” *Advanced Materials*, pp. e08180, 2025.

- [22] Y. Chang, S. Wu, Q. Li, B. Pulli, D. Salmi, P. Yock, J. J. Heit, and R. R. Zhao, “Milli-spinner thrombectomy,” *Nature*, vol. 642, pp. 336-342, 2025.
- [23] Y. Chang, G. Li, J. Sim, G. E. Karniadakis, and R. R. Zhao, “Clot treatment via spinning-induced fibrin microstructure densification and clot volume reduction,” *Extreme Mechanics Letters*, pp. 102391, 2025.
- [24] B. S. Aribisala, Z. Morris, E. Eadie, A. Thomas, A. Gow, M. C. Valdés Hernández, N. A. Royle, M. E. Bastin, J. Starr, and I. J. Deary, “Blood pressure, internal carotid artery flow parameters, and age-related white matter hyperintensities,” *Hypertension*, vol. 63, no. 5, pp. 1011-1018, 2014.
- [25] L. Wexler, D. H. Bergel, I. T. Gabe, G. S. MAKIN, and C. J. MILLS, “Velocity of blood flow in normal human venae cavae,” *Circulation Research*, vol. 23, no. 3, pp. 349-359, 1968.
- [26] J. Carlton, *Marine propellers and propulsion*: Butterworth-Heinemann, 2018.
- [27] S. Wu, W. Hu, Q. Ze, M. Sitti, and R. Zhao, “Multifunctional magnetic soft composites: A review,” *Multifunctional materials*, vol. 3, no. 4, pp. 042003, 2020.
- [28] F. M. White, and J. Majdalani, *Viscous fluid flow*: McGraw-Hill New York, 2006.